Deep Phenotyping of *PDE6C*-Associated Achromatopsia

Michalis Georgiou,[1,2] Anthony G. Robson,[1,2] Navjit Singh,[1,2] Nikolas Pontikos,[1,2] Thomas Kane,[1,2] Nashila Hirji,[1,2] Caterina Ripamonti,[3] Tryfon Rotsos,[4] Alfredo Dubra,[5] Angelos Kalitzeos,[1,2] Andrew R. Webster,[1,2] Joseph Carroll,[6] and Michel Michaelides[1,2]

[1]UCL Institute of Ophthalmology, University College London, London, United Kingdom
[2]Moorfields Eye Hospital NHS Foundation Trust, City Road, London, United Kingdom
[3]Cambridge Research Systems Ltd., Kent, United Kingdom
[4]First Division of Ophthalmology, National and Kapodistrian University of Athens, General Hospital of Athens, Athens, Greece
[5]Department of Ophthalmology, Stanford University, Palo Alto, California, United States
[6]Department of Ophthalmology & Visual Sciences, Medical College of Wisconsin, Milwaukee, Wisconsin, United States

PURPOSE. To perform deep phenotyping of subjects with *PDE6C* achromatopsia and examine disease natural history.

METHODS. Eight subjects with disease-causing variants in *PDE6C* were assessed in detail, including clinical phenotype, best-corrected visual acuity, fundus autofluorescence, and optical coherence tomography. Six subjects also had confocal and nonconfocal adaptive optics scanning light ophthalmoscopy, axial length, international standard pattern and full-field electroretinography (ERG), short-wavelength flash (S-cone) ERGs, and color vision testing.

RESULTS. All subjects presented with early-onset nystagmus, decreased best-corrected visual acuity, light sensitivity, and severe color vision loss, and five of them had high myopia. We identified three novel disease-causing variants and provide phenotype data associated with nine variants for the first time. No subjects had foveal hypoplasia or residual ellipsoid zone (EZ) at the foveal center; one had an absent EZ, three had a hyporeflective zone, and four had outer retinal atrophy. The mean width of the central EZ lesion on optical coherence tomography at baseline was 1923 μm. The mean annual increase in EZ lesion size was 48.3 μm. Fundus autofluorescence revealed a central hypoautofluorescence with a surrounding ring of increased signal ($n = 5$). The mean hypoautofluorescent area at baseline was 3.33 mm^2 and increased in size by a mean of 0.13 mm^2/year. Nonconfocal adaptive optics scanning light ophthalmoscopy revealed residual foveal cones in only one of two cases. Full-field ERGs were consistent with severe generalized cone system dysfunction but with relative preservation of S-cone sensitivity.

CONCLUSIONS. *PDE6C* retinopathy is a severe cone dysfunction syndrome often presenting as typical achromatopsia but without foveal hypoplasia. Myopia and slowly progressive maculopathy are common features. There are few (if any) residual foveal cones for intervention in older adults.

Keywords: adaptive optics, ophthalmoscopy, retinal phenotyping, inherited retinal diseases, genetics, *PDE6C*, achromatopsia, ACHM5

Achromatopsia (ACHM) is an autosomal recessive condition and clinically presents from birth or early infancy with poor visual acuity (VA), pendular nystagmus, photophobia, and reduced or absent color vision loss along all three axes.[1,2] Disease-causing sequence variants have been reported in *CNGA3* (ACHM2, OMIM600053),[3,4] *CNGB3* (ACHM3, OMIM605080),[5] *GNAT2* (ACHM4, OMIM139340),[6,7] *ATF6* (ACHM7, OMIM616517),[8] *PDE6H*[9] (ACHM6, OMIMI610024), and *PDE6C*[10] (ACHM5, OMIM600827). *CNGB3* and *CNGA3* are responsible for 70% of the reported cases and are the most well-studied genotypes, with on-going gene therapy trials (Clinical-Trials.gov numbers NCT03758404, NCT02935517, NCT03001310, NCT02599922, and NCT02610582). A recent study by Weisschuh et al.[11] estimated the prevalence of the *PDE6C* genotype to be 2.4% in a cohort of 1074 independent ACHM families. Due to its low prevalence, a limited number of studies have focused on *PDE6C*-ACHM. In this study, subjects with disease-causing sequence variants in *PDE6C* underwent detailed phenotyping.

The *PDE6C* gene encodes the catalytic alpha subunit of the cone photoreceptor phosphodiesterase, a key regulatory component in cone phototransduction. A homologous mouse model for *PDE6C*-associated ACHM is the spontaneous mouse mutant *cpfl1*, featuring a lack of cone function and rapid, early cone photoreceptor degeneration.[10] In humans, *PDE6C* variants have been reported to cause both complete and incomplete ACHM, cone dystrophy, and cone-rod dystrophy (CORD) in cross-sectional studies.[11–13] Few subjects have been studied longitudinally either as case reports[14] or as part of large genetically heterogeneous cohorts of ACHM/cone dystrophy/CORD.[15–17] No longitudinal study investigating the natural history of *PDE6C* retinopathy has been published to date.

As cone photoreceptors are the target for gene replacement therapies in other forms of ACHM, it is important to assess how the cones are affected by *PDE6C* sequence variants to thereby better understand the potential for future functional rescue. A variety of noninvasive imaging tools are available for examining retinal structure, and they have been applied extensively to the more common forms of ACHM.[18-20] Optical coherence tomography (OCT) provides visualization of retinal lamination, enabling measurements of the integrity of the ellipsoid zone (EZ) and individual layer thickness. In the cone dysfunction syndromes, of particular interest are the hyperreflective (EZ and interdigitation zone) and hyporeflective (outer nuclear layer [ONL]) bands associated with photoreceptors.[21,22] In patients with *CNGA3*- or *CNGB3*-ACHM, the EZ band is disrupted or absent in about 70% of cases.[19,20] The thickness of the ONL is also significantly reduced in *CNGA3*- and *CNGB3*-ACHM, although there is substantial variability between subjects.[20,23] No study to date has longitudinally investigated OCT structure in a cohort of *PDE6C*-ACHM.

Confocal and nonconfocal adaptive optics scanning light ophthalmoscopy (AOSLO) have been used for in-depth phenotyping in inherited retinal diseases.[24] AOSLO allows for noninvasive, cellular-resolution imaging of the rod and cone photoreceptor mosaic.[25-27] In patients with *CNGA3* or *CNGB3*-ACHM, there is an absence of normally waveguiding cone photoreceptors in confocal AOSLO (presenting as "dark spaces"),[18,20] although the rod photoreceptor mosaic appears normal (Patterson E, et al. *IOVS* 2018;59:ARVO E-Abstract 652). Using a nonconfocal AOSLO technique, a remnant inner segment structure has been observed in these patients that spatially coincides with the nonwaveguiding cones seen in the confocal image.[20,28] Nonconfocal AOSLO has thereby allowed the identification of a cone inner segment structure in these spaces.[29,30] This identification of cellular targets has underpinned the design and participant selection for planned and on-going gene therapy trials of *CNGA3* and *CNGB3*-ACHM. Despite the characterization of *CNGA3*-, *CNGB3*-, and the rare *ATF6*- and *GNAT2*-ACHM, there are no reports of AOSLO data from patients with *PDE6C*-ACHM. The current study aims to examine the foveal cone mosaic, possible perifoveal rod involvement, and variation between patients using AOSLO.

In addition to the limited structural characterization of *PDE6C*-ACHM, investigations of the functional phenotype have also been limited. Comprehensive data are lacking on electroretinography (ERG), color vision, and natural history. This study details these phenotypic characteristics and examines the potential for functional rescue compared with other forms of ACHM.

METHODS AND MATERIALS

The study was approved by the ethics committee of Moorfields Eye Hospital. Written informed consent was obtained from all subjects attending the research appointment after explanation of the nature and possible consequences of the study. The research followed the tenets of the Declaration of Helsinki.

Subjects

Eight subjects from eight independent pedigrees with likely disease-causing sequence variants in *PDE6C* were identified in the genetics database of Moorfields Eye Hospital, London, UK. All subjects were invited for a research appointment including AOSLO imaging. One subject could not attend due to unrelated healthcare problems and another was based abroad. Six of the subjects were recruited and attended a detailed research visit,

and the available data of all eight subjects were used for evaluating the natural history of the condition.

Genetics

All eight patients were screened for 176 genes associated with retinal dystrophy by next-generation sequencing; *PDE6C* variants were confirmed by Sanger sequencing (OMIM*600827) in the Manchester Centre for Genomic Medicine, Manchester, United Kingdom.

Spectral-Domain OCT (SD-OCT)

SD-OCT imaging was performed on both eyes, following cycloplegia and pupillary dilation with 1% tropicamide and 2.5% phenylephrine eye drops. Horizontal line and volume scans were acquired with the Spectralis device (Heidelberg Engineering, Heidelberg, Germany) by using the same protocol as that used by Aboshiha et al.[16] In addition, the device was used in follow-up mode so that the same scanning location was imaged at follow-up and baseline. To address difficulties caused by nystagmus, the methods described by Tee et al.[31] were used to ensure serial analysis of the same subject-specific retinal location. The foveal center is identified on the baseline transfoveal OCT image, and the corresponding point is marked on the accompanying baseline near infrared reflectance (NIR-R) fundus image. The baseline NIR-R overlay was copied and pasted on the final NIR-R fundus image as per vendor software after aligning them. The vertical OCT marker position on the final image is then adjusted to correspond to that shown on the final NIR-R image so the line scan over the exact same location is identified.

The extent of the central EZ disruption was measured after marking the nasal and temporal boundaries of the EZ lesion by using digital callipers (Heidelberg Eye Explorer; Heidelberg Engineering) and a 1-μm:1-μm display with maximum magnification. All OCT measurements were performed by the same examiner (MG). The transverse scale of each image was calculated using the axial length of the corresponding eye when available. This was measured using the Zeiss IOL Master (Carl Zeiss Meditec, Dublin, CA, USA) for the six subjects who attended a research appointment. The same axial length measured on the last follow-up was used also to correct the baseline scans (all subjects were adults at baseline imaging, and axial length was therefore assumed to be constant). The ONL thickness was calculated as the distance between the internal limiting membrane and the external limiting membrane also by using the digital callipers.

Qualitative assessment of the foveal structure was performed by grading SD-OCT images into one of five categories as previously reported by Sundaram et al.[19]: (1) continuous EZ, (2) EZ disruption, (3) EZ absence, (4) presence of a hyporeflective zone, or (5) outer retinal atrophy. For each subject, both right and left eyes were graded at baseline and follow-up. Consensus grading was established by three independent observers (NH, MG, and MM). The presence/absence of foveal hypoplasia was also noted and defined as the persistence of one or more inner retinal layers (outer plexiform layer, inner nuclear layer, inner plexiform layer, or ganglion cell layer) through the fovea.[32] The prevalence of foveal hypoplasia was compared with the reported prevalence in the literature.

Fundus Autofluorescence (FAF)

The earliest and the latest available FAF imaging for each eye were used as baseline and follow-up, respectively. FAF imaging was performed using the FAF mode on the Spectralis device (Heidelberg Engineering), following pupillary dilation and after

SD-OCT image acquisition. All FAF images were examined for the pattern of autofluorescence and the presence of a hyperautofluorescent ring. In subjects displaying a well-demarcated region of reduced autofluorescence, the area was measured by tracing the circumference of the hypoautofluorescent central region with a mouse-driven cursor and recording the area within, as calculated by image analysis software (Heidelberg Eye Explorer; Heidelberg Engineering). The ring area of the increased signal was calculated by subtracting from the area delineated by the outer border of the hyperautofluorescent ring the aforementioned central area of reduced autofluorescence. All FAF measurements were made by a single observer (MG).

Electroretinography

Six patients (age range, 20–42 years) had undergone international standard full-field ERG and pattern ERG testing[33,34] and five had additional short-wavelength flash (S-cone) ERG testing (stimulus duration 5 ms)[35] at Moorfields Eye Hospital. All available ERG data were reviewed by a consultant electrophysiologist (AGR).

Color Vision Tests

Patients underwent testing with Hardy-Rand-Rittler pseudoisochromatic plates (AO-HRR, 4th edition; Richmond Products, Inc., Albuquerque, NM, USA). AO-HRR plates were presented under a Daylight Illuminator (Richmond Products, Inc.) and scored using the accompanying worksheet.

A commercially available low-vision version of the Cambridge Colour Test (lvvCCT) trivector version was performed using the Metropsis system (Cambridge Research Systems Ltd., Rochester, Kent, UK). The test stimuli were presented on a calibrated 32-inch monitor, with a refresh rate of 120 Hz, 1920 × 1080-pixel spatial resolution, and up to 16-bit (per channel) color resolution. The stimuli consisted of four homogeneous discs presented simultaneously on a 2-cd/m^2 neutral background in a diamond-shaped array. Each disc subtended 4 degrees and was separated by 2.5 degrees from the adjacent discs. The viewing distance was 150 cm. On each presentation, one of the discs differed in chromaticity from the remaining three, which remained of neutral hue. The patient was instructed to report which of the four discs was different in color[36] by pressing the corresponding key on a five-key RB-540 Cedrus response box (Cedrus, San Pedro, CA, USA). Color discrimination was probed along the protan, deutan, and tritan confusion axes. For each axis, the corresponding saturation of the color disc would decrease or increase according to whether the patient answered correctly or incorrectly to the previous trial, respectively. More information on the adaptive procedure used by the lvvCCT is described in Simunovic et al.[36] On completion of the test, the lvvCCT returned the saturation threshold along each confusion axis, which represents the minimum saturation required to discriminate the color disc from the achromatic discs. Both color vision tests were performed monocularly.

AOSLO Imaging of the Photoreceptor Mosaic

High-resolution imaging was attempted in six subjects by using a previously described custom-built AOSLO[37] at Moorfields Eye Hospital/UCL Institute of Ophthalmology, London, UK. Imaging with confocal, split detection (nonconfocal), and dark field was performed.

Pupil dilation and cycloplegia were achieved as described for OCT. Images were obtained over the central retina and in strips extending from the fovea to 10 degrees in the temporal and superior directions. Image sequences were recorded as AVI files of 150 frames, either at a 1° and/or 1.5° square field of view. A desinusoiding algorithm was applied to each image sequence, and individual frames were selected,[38] registered,[39] and averaged to increase the signal-to-noise ratio for subsequent analysis. The final images were combined into a single montage (Adobe Photoshop; Adobe Systems, Inc., San Jose, CA, USA) in layers for the different detection schemes by using a custom-built automated software.[40] The scale was determined first in degrees per pixel in an image of a Ronchi ruling of known spacing, after each imaging session. Then, the value was linearly scaled by using the subject's axial length. Peak cone density was used for quantitative assessment of AOSLO imaging as previously described,[23] and the mosaics were also qualitatively characterized.

Statistical Methods

Statistical analysis was performed with IBM SPSS Statistics for Windows (version 22.0; IBM Corp., Armonk, NY, USA).

RESULTS

Demographics and Genetics

Eight subjects were ascertained, of which seven were female. All subjects were unrelated and represent independent pedigrees. Five of the subjects had homozygous variants and were from consanguineous pedigrees. Ten different variants were identified, with only one splicing defect (c.864+1G>A) being identified in two pedigrees (homozygous and compound heterozygous). Of the 10 variants, 2 were nonsense, 6 missense, and 2 insertions leading to splicing defects. The Combined Annotation Dependent Depletion score is above 20 for all variants, indicative of pathogenicity (Supplementary Material).[41] Three variants, namely, p.(Glu109Val), p.(Leu298-His), and p.(Gly835Ter), are novel, not found in gnomAD exomes/genomes despite good coverage, and not reported in Clinvar. To the best of our knowledge, only one of the variants has been previously subject to a published phenotype study [p.(Arg102Trp)].[11,19] No other homozygous or heterozygous variants likely to modify or influence the retinal phenotype were identified, and none were found in any other genes associated with ACHM. The age of baseline examination was not the same for all tests, and follow-up periods varied (baseline data were obtained retrospectively). For each test, the mean age, age range, and follow-up time are reported individually. Demographics and genetics are summarized in the Table.

Clinical Presentation

All subjects presented with early-onset fine nystagmus, decreased VA, light sensitivity, and severe color vision loss. None of the patients could recall any color discrimination. A common feature for all subjects was refractive error, with high myopia (>6 diopters) in five patients (62.5%), mild hyperopia in two patients (25%), and myopic astigmatism in one patient (12.5%). Axial length was available for the subjects who underwent AOSLO imaging ($n = 6$). The four subjects with high myopia had a mean axial length of 27.29 mm (range, 26.85–27.67 mm) and the remaining two had mild hyperopia with a mean axial length of 22.72 mm (range, 22.53–22.91 mm).

Mean baseline age (±SD, range) was 30 years (±10.7, 10–45) and mean follow-up (range) was 10 years (1.7–15.9 years). Longitudinal VA data were available for all patients. Mean VA (±SD) for both eyes at baseline was 0.92 LogMAR (±0.11),

Investigative Ophthalmology & Visual Science

TABLE. Demographics, Genetics, and Phenotyping Data

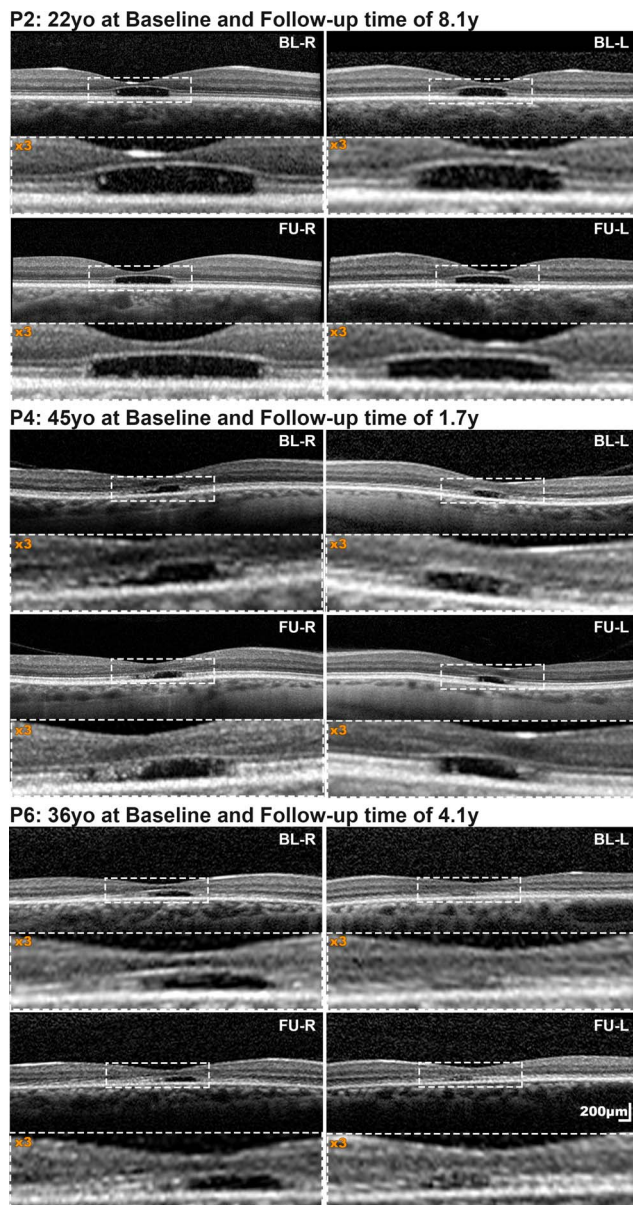| Subject	Sex	Pedigree	Ethnic Group	Variant 1 / Variant 2 (cDNA, Protein)	Eye	Axial Length (mm)	Visual Acuity (LogMAR)	Spherical Equivalent	Age BL (y)	FU Time (y)	EZ Grade*	EZW loss BL (µm)	EZW Rate of Loss (µm/y)	Age BL (y)	FU Time (y)	Rate of Increase in DAF (mm²/y)	Rate of Ring Increase (mm²/y)	Evidence of Progression
											OCT					FAF		
P1	F	GC23489	Nepali	c.864+1G>A, Slicing Defect / c.311G>A, p.Arg104Gln	R	NA	1.0	−3.75	26	NA	3	1058	NA	NA	NA	NA	NA	NA
					L	NA	1.0	−3.75			NA	NA	NA			NA	NA	
P2	F	GC17774†	Pakistani	c.864+1G>A, Slicing Defect / c.864+1G>A, Slicing Defect	R	22.86	1.0	+2.25	22	8.1	4	671	4	25	4.2	0.03	0.01	No
					L	22.95	1.0	+2.25			5	612	9			0.02	0.01	
P3	F	GC18349†	Pakistani	c.631G>T, p.Glu211Ter/ c.631G>T, p.Glu211Ter	R	22.50	0.78	−0.50	29	7.3	5	2053	102	27	5.9	0.19	0.10	Yes
					L	22.56	0.78	−0.50			5	1866	107			0.15	0.10	
P4	F	GC23440	British White	c.893T>A, p.Leu298His / c.326A>T, p.Glu109Val	R	26.77	0.60	−10.25	45	1.7	4	641	2	44	1.7	0§	0§	No
					L	26.92	0.72	−11.00			4	594	1			0§	0§	
P5	F	GC18730†	Pakistani	c.2503G>T, p.Gly835Ter / c.2503G>T, p.Gly835Ter	R	NA	1.0	−10.50	36	2.7	5	4087	175	32	5.9	0.30	0.13	Yes
					L	NA	1.0	−11.00			5	4065	178			0.20	0.09	
P6	F	GC16890†	Pakistani	c.1646T>C, p.Met549Thr / c.1646T>C, p.Met549Thr	R	26.95	1.0	−14.00	36	4.1	4	503	2	35	3.1	0§	0§	No
					L	27.06	0.89	−14.50			4	452	3			0§	0§	
P7‡	M	GC18529†	Pakistani	c.304C>T, p.Arg102Trp / c.304C>T, p.Arg102Trp	R	27.88	1.0	−11.00	42	8.3	5	2512	43	41	9.0	0.12	0.16	Yes
					L	27.45	1.0	−12.00			5	2971	54			0.28	0.15	
P8	F	GC19847	British White	c.595A>G, p.Lys199Glu / c.1847+3_1847+6delAAGT, Splicing Defect	R	27.78	1.0	−9.00	46	7.3	5	3861	11	45	7.3	0.03	0.27	Yes
					L	27.47	1.0	−9.75			5	4149	47			0.03	0.17	

BL, baseline; FU, follow-up; EZW, EZ width; NA, not available; DAF, decreased autofluorescence; LogMAR, logarithm of the minimum angle of resolution.

* Grading system as previously published.[19]
† Consanguineous cases, parents were cousins and patients homozygous for the variant.
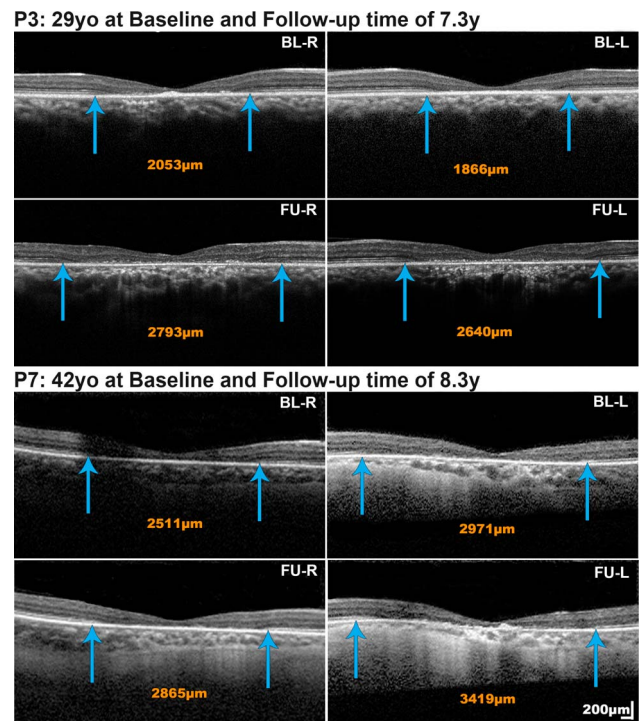‡ Previously reported patient.[11,19]
§ Subjects without area of DAF and without a ring of increased signal.

P2: 22yo at Baseline and Follow-up time of 8.1y

P4: 45yo at Baseline and Follow-up time of 1.7y

P6: 36yo at Baseline and Follow-up time of 4.1y

FIGURE 1. Spectral-domain optical coherence tomography (SD-OCT) in cases with minimal change over time. For all patients, both baseline and follow-up horizontal transfoveal scans are presented at the same scale. The central area marked with a *dashed white rectangle* is magnified (×3), below each scan. All three subjects had a grade 4 EZ (presence of hyporeflective zone) both at baseline and follow-up, confined to the fovea, with minimal increase in the EZ lesion size of 3.54/8.87, 2.01/0.68, and 1.65/2.76 μm/year for right/left eyes of P2, P4, and P6, respectively. BL-R, baseline right eye; BL-L, baseline left eye; FU-R, follow-up right eye; FU-L, follow-up left eye; y, years; yo, years old.

P3: 29yo at Baseline and Follow-up time of 7.3y

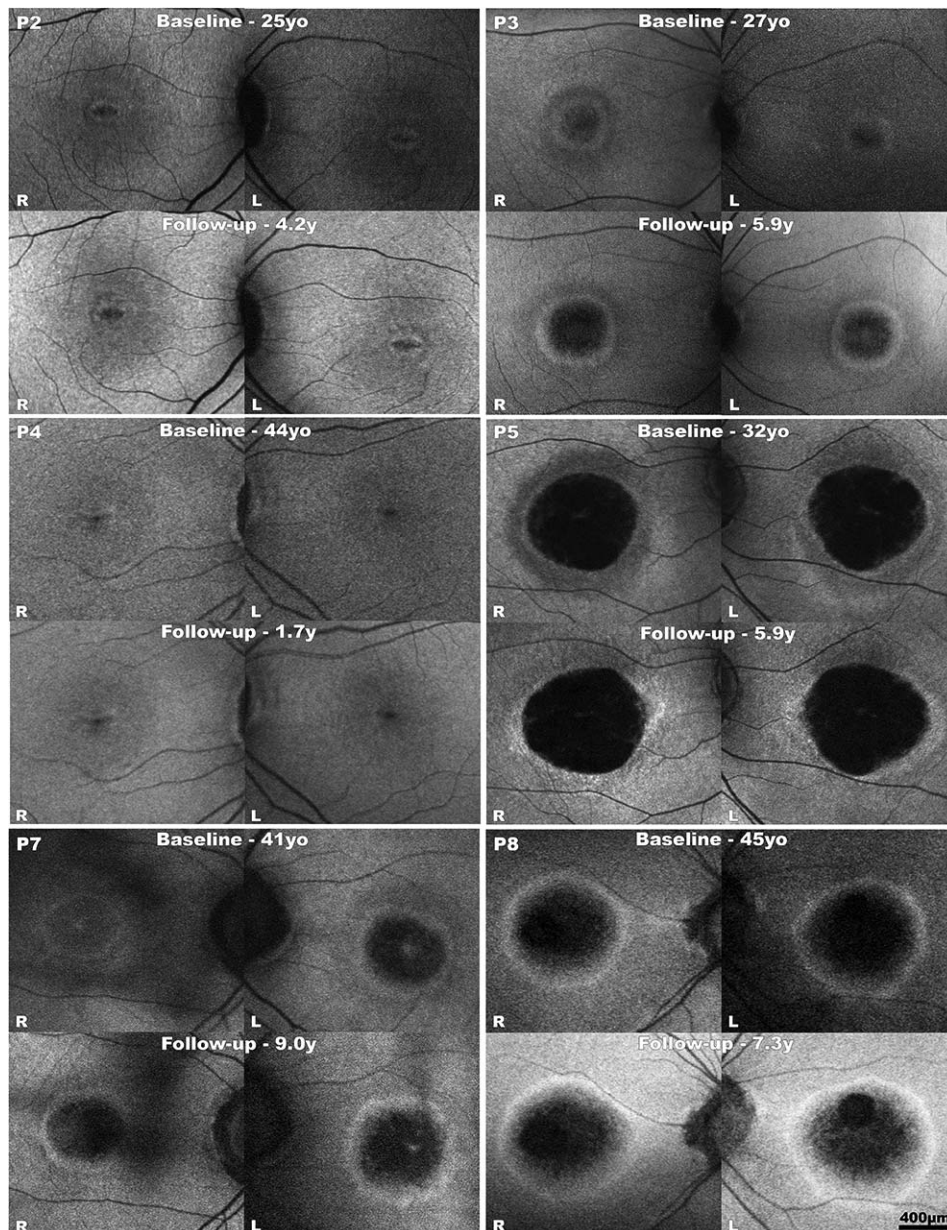**P7: 42yo at Baseline and Follow-up time of 8.3y**

FIGURE 2. Spectral-domain optical coherence tomography (SD-OCT) in cases with progression over time. The nasal and temporal border of the EZ lesion are marked with *blue arrows* and in the extent of the lesion reported in *orange numbers*. The size of the EZ lesion increased in P3 and P7 at rates (right eye/left eye) of 102.02/106.71 μm/year and 42.52/53.67 μm/year, respectively. *Scale bars* = 200 microns, with all scans at the same scale.

Spectral-Domain OCT

No subject had a residual EZ at the foveal center; one subject had an absent EZ (grade 3), three had a hyporeflective zone (grade 4), and four had outer retinal atrophy. The width of the EZ lesion at baseline was 1923 μm (range, ± SD; 503–4087 μm, ±1359 μm). Mean age ± SD at baseline OCT was 36 ± 8 years. One patient (P1) attended only once with only the OCT from the right eye included for quantification; nystagmus precluded accurate scanning of the left eye through the foveal center. Foveal hypoplasia was absent in all *PDE6C* subjects. In contrast, in previous ACHM cohorts, foveal hypoplasia was a common finding. Ninety-seven of 146 previously reported subjects with *CNGA3*- and *CNGB3*-ACHM[15,18–20,42] and all 21 reported subjects with *ATF6*-ACHM had foveal hypoplasia (Fisher's exact test, $P = 0.0003$).[8,32,43]

Seven patients had a mean follow-up of 5.6 years for OCT (range, 1.7–8.3 years). The mean (range, ± SD) annual rate of increase in EZ lesion size was 48.3 μm (1.7–178, ±61.7), with all subjects progressing at highly variable rates. Patients P2, P4, and P6 showed minimal if any change (Fig. 1; Table). In contrast patients P3, P5, P7, and P8 progressed, however, at different rates, with the two younger subjects (P3 and P5; Fig. 2, P3) progressing faster than the two older subjects (P7 and P8; Fig. 2, P7). The rate of progression was similar between eyes ($P = 0.123$, t = −1.794, df = 6). Reduced foveal ONL thickness was observed in all four subjects without atrophy (mean ONL thickness ± SD; 51.75 ± 6.98 μm for the right eye of patients P1, P2, P4, and P6 at last follow-up; Fig. 1). No further thinning was observed over time (Fig. 1, P2, P4, and P6). The Table summarizes OCT-related measurements.

ranging from 0.72 LogMAR to 1.0 LogMAR and at follow-up was 0.89 LogMAR (±0.14), ranging from 0.72 LogMAR to 1.0 LogMAR. Best-corrected VA was stable over time ($P = 0.399$, t = 0.899, df = 7). Six patients (P1–P6) reported stable vision with no new visual complaints. Two patients (P7 and P8) reported worsening of their central vision in their mid-40s. Patient P6 also reported a reduction in central vision in her late 20s, with worsening photoaversion and a preference for darker tinted spectacles.

FIGURE 3. Fundus autofluorescence (FAF) images at baseline and follow-up for both eyes of six patients. P2, P3, P5, P7, and P8 have a central area of hypoautofluorescence with a surrounding ring of increased signal. Both the area of atrophy and the ring of increased signal are expanding at comparable rates from the foveal center to the periphery. The rate, however, was variable among subjects, with patients P2 and P7 progressing minimally, if at all. P4 has a normal-appearing FAF at baseline and follow-up, with subtle foveal changes. All images are at the same scale. R, right eye; L, left eye

Fundus Autofluorescence

Previously, Aboshiha et al.[16] reported three patterns of FAF in ACHM: (1) reduced central signal, (2) normal, and (3) increased central signal. In this cohort, FAF was available for all patients and none of the patients had increased signal centrally. Three patients had normal FAF (P1, P4, and P6). Patients P4 and P6, as mentioned previously, also had relatively stable OCT findings; and P1 was the only patient with a grade 3 EZ on OCT.

A central well-defined area of hypoautofluorescence with a surrounding ring of increased signal was present in five subjects (P2, P3, P5, P7, and P8; mean age $\pm$ SD, 34 $\pm$ 7.8 years) who had a mean follow-up of 6.5 years (Fig. 3). The mean hypoautofluorescent area at baseline was 3.33 mm^2 and

3.78 mm^2 for right and left eye, respectively, and increased in size by a mean of 0.13 mm^2/year and 0.15 mm^2/year, respectively. Both the baseline area of hypoautofluorescence ($P = 0.135$, t = -1.869, df = 4) and the annual rate of progression ($P = 0.977$, t = -0.031, df = 4) were similar between eyes. The mean area of the hyperautofluorescent ring at baseline was 2.03 mm^2 and 2.21 mm^2 for right and left eye, respectively, and increased centrifugally at a similar rate ($P = 1.66$, t = -1.692, df = 4) of 0.14 mm^2/year and 0.10 mm^2/year, respectively. Both the area of atrophy and the ring of increased AF expanded at comparable rates from the foveal center to the periphery. The rate, however, was variable between subjects, with patients P2 and P7 progressing minimally if at all. For P7, one of the oldest patients in the cohort, the rate of OCT progression was also minimal. The other patient that had

minimal change in OCT was P8; however, there was evidence of progression on FAF, which may be due to the area of decreased signal and the edge of the hyperautofluorescent ring not being well defined on FAF images (Fig. 3, P8). The Table summarizes the FAF measurements.

Electroretinography

Pattern ERGs were undetectable in five of five cases (age range, 20–42 years old) and technically unsatisfactory in one due to severe nystagmus. The dark-adapted (DA) strong flash (DA10) ERG a-waves were normal or mildly subnormal, with one older case (P8) with the greatest axial length showing the greatest (50%) reduction (Figs. 4 and 5A); the mean a-wave amplitude was 33% lower than the mean for a control group of 130 unaffected individuals. The DA10 ERG a- and b-wave peak times were within normal limits (Fig. 5B). Light-adapted (LA) 30-Hz flicker ERGs were undetectable ($N = 5$) or residual ($N = 1$). Single flash cone (LA3) ERG b-waves were detectable but delayed, and the mean amplitude was reduced by 90% compared with that for the control group. The LA3 ERG waveforms resembled those for S-cone ERGs (Figs. 4 and 5C). The S-cone ERGs had a slightly simplified or monophasic waveform shape but fell within the normal amplitude range,[44] in all but one individual (P6) with a borderline response (Fig. 4).

Color Vision Tests

All patients underwent AO-HRR plate testing, and they were able to correctly identify only the test plates. Five patients underwent the low vision version of the Cambridge Colour Test at the last follow-up, including three with detectable S-cone ERGs. All of them scored the maximum or near-maximum saturation allowed by the test. No color discrimination was detected along any of the confusion axes in any patient.

AOSLO Imaging of the Photoreceptor Mosaic

Two of the six subjects that underwent AOSLO imaging had montages that were analyzable and of an adequate image quality. The confounding factors for successful image acquisition were nystagmus, high refractive error (P6, grade 4 EZ on OCT), and a large area of atrophy in which no structure could be identified (P3, P7, and P8; all with grade 5 EZ on OCT). AOSLO was analyzable in patients P2 and P4. Both patients had relatively stable disease and grade 4 EZ on OCT, with P2 having a small hyperautofluorescent ring (Fig. 3, P2) and patient P4 a normal FAF (Fig. 3, P4).

Patient P2 Mosaic. A central dark atrophic region was imaged with a lack of waveguiding properties by using confocal AOSLO, and ambiguous cellular structures (remnant inner segments) were identified on nonconfocal split-detection (Fig. 6). This is in direct contrast to other forms of ACHM where inner segments are visible on split-detection over the foveal center. Outside the foveal center, black spaces in the confocal images corresponded to inner segments evident in the split detection mode, as in *CNGA3-* and *CNGB3-*ACHM. Cells along the edge of the lesion had preserved waveguiding properties and corresponding inner segments on split-detection (Figs. 6B, 6C).

Patient P4 Mosaic. The central imaged area, including the foveal center, was hyperreflective over most of its area, with a small hyporeflective region temporally on confocal AOSLO (Fig. 7A). The hyperreflective area was consistent with atrophic changes, as previously reported for *ATF6-*ACHM,[32] with no visible inner segments on split-detection. In contrast, in the hyporeflective island, inner segments were identified on

split-detection, similar in appearance to *CNGA3-* and *CNGB3-*ACHM (Fig. 7B). The peak cone density was calculated as 11,895 cone/mm^2. Previous studies reported a mean peak cone density (range) of 19,844 (6,574–54,785) cones/mm^2, 21,373 (7,273–53,554) cones/mm^2, and 130,508 (84,733–165,080) cones/mm^2 for *CNGA3-*ACHM,[23] *CNGB3-*ACHM,[20] and healthy controls,[45] respectively. In the periphery, as in patient P2, black spaces were identified on confocal imaging, corresponding to observed inner segments on split-detection. The signal-to-noise ratio on confocal imaging was low, but there was evidence of some cones showing waveguiding properties (Fig. 7).

Discussion

This study details the deep phenotyping of a series of patients with the rare form of *PDE6C*-associated ACHM, including cross-sectional and longitudinal analyses of structural and functional features. The clinical presentation, OCT, FAF, ERG, color vision, and, uniquely for this disorder, AOSLO imaging with confocal and split-detection were examined. The findings indicate that *PDE6C* retinopathy has a distinct natural history and features that differ from other forms of ACHM, which is of relevance to clinical management and the potential for future therapeutic intervention.

The full-field ERGs showed evidence of severe generalized cone system dysfunction but with a relative preservation of short-wavelength sensitivity, as seen previously in one other rare form of ACHM (*GNAT2*),[46] and resembling the findings in blue cone monochromacy.[47] The similarity of waveform shape between the markedly reduced LA3 ERG and relatively preserved S-cone ERG suggests a possible common origin. The DA10 strong flash ERG abnormalities (Figs. 4, 5A) may largely be explained by a loss of the DA cone system contribution and high myopia, but an additional loss of rod photoreceptor function may occur in some older individuals (patient P8, with ERG at 38 years of age). Pattern ERG P50 was undetectable, consistent with macular dysfunction, although it is possible that attenuation was partly attributable to the effects of nystagmus. In confocal AOSLO imaging, some waveguiding cones were identified. However, the presence of those cells and the residual S-cone ERG recordings did not translate to residual color discrimination in any of the patients, either with color vision testing or reported by the patients, a finding also in common with a previously reported patient with *GNAT2-*ACHM.[46] A contributing factor for the color vision findings in the *PDE6C* patients may be the presence of maculopathy evident on OCT and FAF. Full-field ERGs have minimal contribution from the central macula and reflect generalized (peripheral) retinal function (full-field ERGs typically remain normal if dysfunction is confined to the macula). The lack of correlation may also relate to fundamentally different test paradigms; conventional color vision tests assess central rather than peripheral color vision and measure color thresholds or color discrimination thresholds at the macula, rather than suprathreshold responses from the periphery (as for ERG). Another explanation might be that the color vision test lacked the required sensitivity. More detailed color vision testing will be of value to further establish any residual color discrimination.

The FAF findings in older patients revealed areas of macular atrophy. The atrophy extended beyond the rod-free region (Fig. 3, P5, P7, and P8). Stearns et al.[48] reported a blind zebrafish mutant with rapid degeneration of cone photoreceptors caused by a disease-causing variant in *PDE6C* and a limited amount of rod degeneration, primarily in areas with a low density of rods. They proposed that rod photoreceptors in
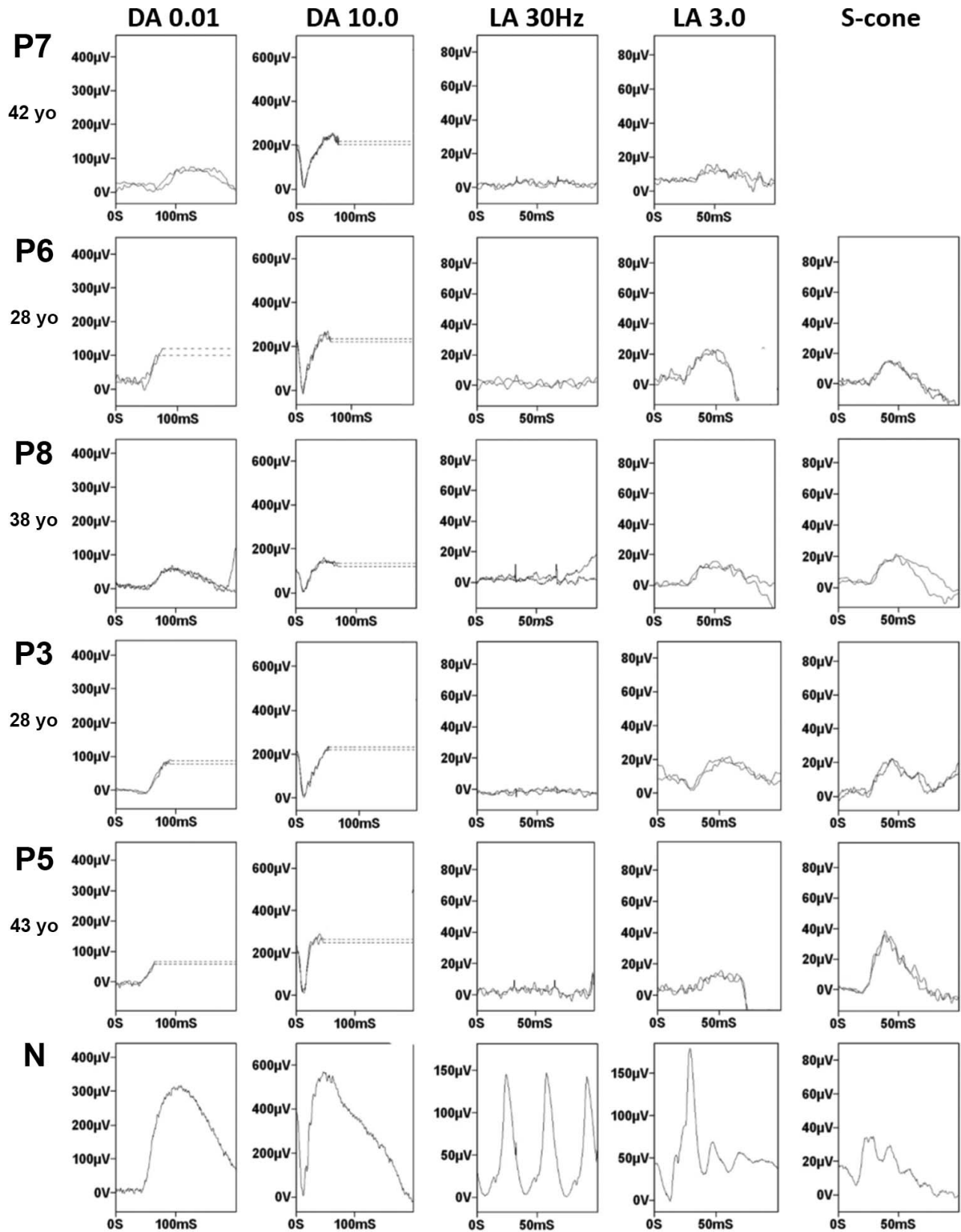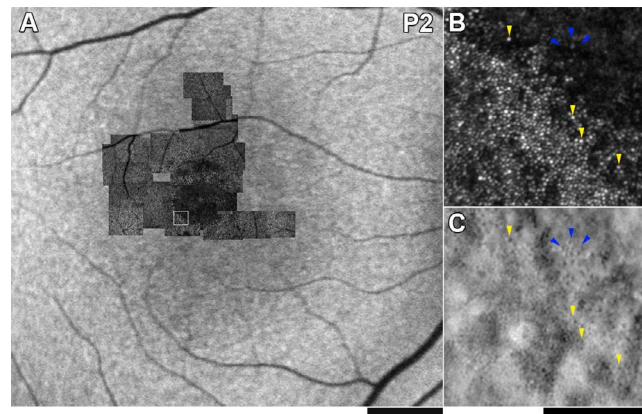
FIGURE 4. International-standard full-field ERGs and S-cone ERGs recorded from five subjects and one representative control subject for comparison (N). Data are shown for one eye but all had symmetrical responses. Broken lines replace blink/eye movement artefacts related to nystagmus, for clarity. Note increased amplitude scaling of LA 30 Hz and LA3 ERGs in the patients compared with the control. The DA10 ERG a-waves were normal or mildly subnormal, with a tendency to be smaller in older subjects (P7 and P8). The mean a-wave amplitude was decreased. Single flash cone (LA3) ERG b-waves were detectable but delayed, simplified, and reduced. The LA3 ERG and S-cone ERG waveforms were similar (see text for details).
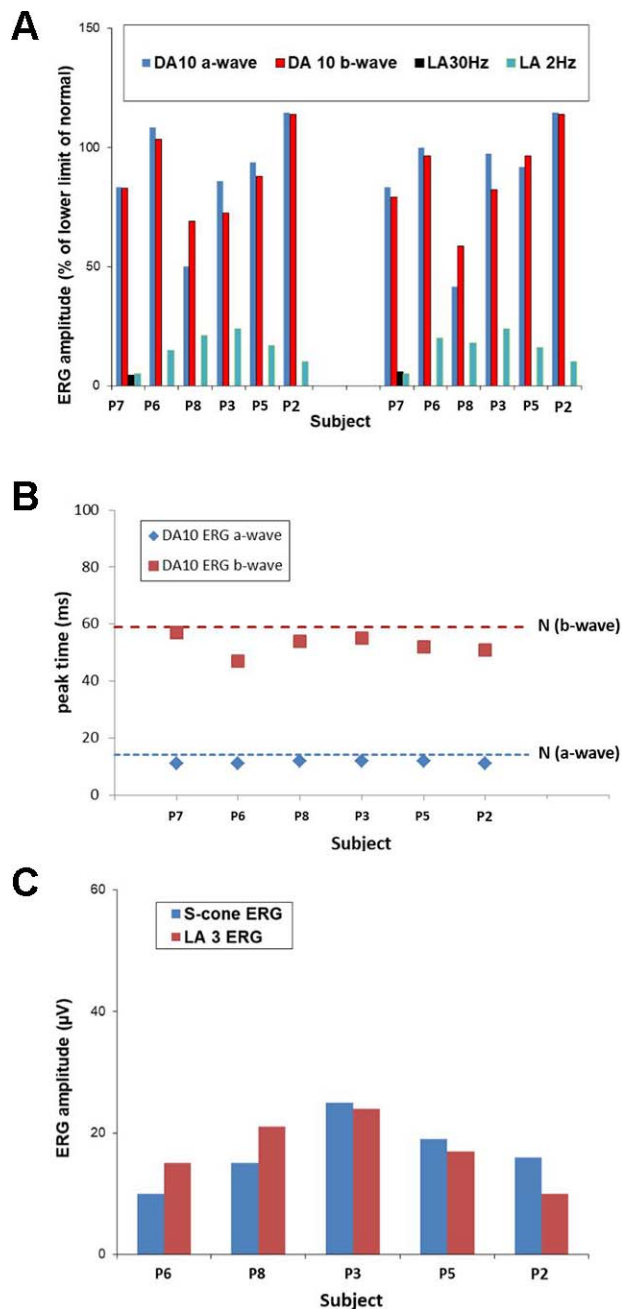
FIGURE 5. ERG graphs. (**A**) The mean a-wave amplitude was 33% lower than the mean for a control group of 130 unaffected individuals. Light-adapted (LA) 30-Hz flicker ERGs were undetectable or residual (P7). (**B**) and (**C**) show data from right eyes. (**B**) The DA10 ERG a- and b-wave peak times were within normal limits. (**C**) The LA3 ERG and S-cone ERG amplitudes were similar. The lower limit of normal amplitude for the LA3 ERG is 101 μV and that for the S-cone ERG is 10 μV.[44]

FIGURE 6. Adaptive optics scanning light ophthalmoscopy (AOSLO) of P2. (**A**) Confocal AOSLO photoreceptor mosaic scaled and superimposed on an FAF image. A central dark atrophic region was imaged, revealing a lack of waveguiding properties. The *white square* marks the 200-μm square in greater magnification in (**B**). (**B**) Confocal imaging and (**C**) split-detection image over the same location. The top right corner lacks waveguiding properties on (**B**) and ambiguous cellular structures (*blue arrow heads*, remnant inner segments) are seen on split-detection (**C**). A few cones at the edge of the lesion have greater preserved reflectivity, and inner segments on split-detection and are marked with *yellow arrowheads*. *Scale bar* for (**A**), 1000 μm; and for (**B**, **C**), 100 μm

areas of the retina with a high density of rods are protected from degeneration, concluding that cell density plays a role in determining whether rod photoreceptors degenerate as a secondary consequence to cone degeneration. In contrast, the homologous mutant *cpfl1* mouse model for *PDE6C*-ACHM is characterized by only a lack of cone function, with rapid, early cone photoreceptor degeneration.[10] Variants in *PDE6C* have also now been associated with CORD in one patient in a recent genotyping study in a large ACHM cohort.[11] The reported patient was among the oldest in that ACHM cohort (33 years

old), and the diagnosis was reclassified from ACHM to CORD. In our cohort, all patients meet the clinical criteria of ACHM, including decreased VA, photoaversion, no color discrimination, and nystagmus from birth/early infancy. A distinct additional feature was refractive error observed in all patients, with high myopia in the majority. Blue cone monochromacy (BCM) presents similarly to ACHM, with severely reduced color discrimination and visual acuity, photophobia, and nystagmus in affected males (X-linked disease).[2] High myopia and relatively preserved S-cone ERGs (common features of both *PDE6C*-ACHM and BCM) may mislead into the diagnosis of BCM in male *PDE6C* patients. A distinguishing factor between ACHM and BCM is that subjects with BCM have residual tritan color discrimination.[49] Molecular genetic testing will help to confirm the correct diagnosis. Based on the findings of the study herein, three patients can be classified as having stationary disease (P1, P4, and P6), but cases P3, P5, P7, and P8 showed evidence of progressive macular atrophy, with possible peripheral rod system involvement in case P8. Interestingly, none of our patients reported rod-related problems (e.g., nyctalopia), all preferred mesopic conditions, and all were photoaverse. Any rod involvement appears to be minimal and late in the disease course.

In the on-going debate about the stationary or progressive nature of ACHM, *PDE6C* patients should be studied individually. ACHM studies with different proportions of *PDE6C* patients have shown conflicting results.[15,17] Thiadens et al.,[15] in a cohort with five *PDE6C* patients (20%), concluded that ACHM was often a progressive disease. Hirji et al.,[17] in a cohort with one *PDE6C* subject (2%), concluded that ACHM was predominantly stationary. In the latter study, the single patient with *PDE6C* also showed a change in the area of reduced FAF, which was greater than the total change of the other 17 patients with decreased autofluorescence and different ACHM genotypes (*CNGA3*, *CNGB3*, and *ATF6*).[17] The presence of a hyperautofluorescent ring (Fig. 3) in five patients is a feature not previously described in *PDE6C*-ACHM or other ACHM genotypes. Robson et al.[50] demonstrated that increased FAF in CORD was associated with reduced rod and cone sensitivity,

Investigative Ophthalmology & Visual Science
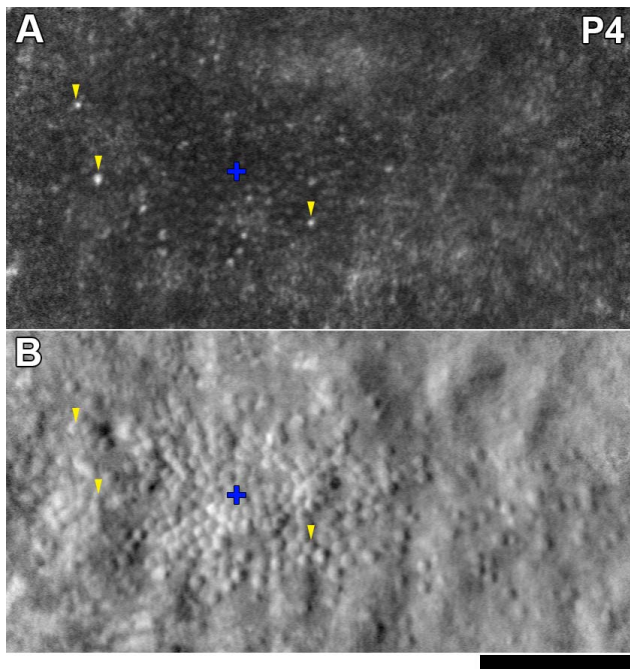
FIGURE 7. Adaptive optics scanning light ophthalmoscopy (AOSLO) of P4. (**A**) Confocal image over the fovea with lack of normal waveguiding properties. Few bright spots, which may be waveguiding cones, are marked with *yellow arrowheads*. (**B**) Split-detection AOSLO over the exact same location reveals an island of residual inner segments. The *yellow arrowheads* mark the same location as in (**A**) and the bright spots on confocal appear to have corresponding inner segments. The *blue cross* marks the location of the calculated peak cone density (11,895 cones/mm^2). *Scale bar*: 100 μm

with scotopic sensitivity reductions being milder than photopic losses. Another notable difference between *PDE6C* and other genotypes of ACHM is the normal inner retinal lamination. Previous studies have found foveal hypoplasia in all patients with *ATF6*-ACHM[8,32,43] and in most of the patients with *CNGA3* and *CNGB3*-ACHM.[17,20,23] The other form of ACHM without foveal hypoplasia is *GNAT2*-ACHM.[46] However, *GNAT2*-ACHM most commonly presents with a continuous EZ,[16] in direct contrast to *PDE6C*-ACHM, in which all the patients have grade 3 to 5 EZ changes.[11-13]

AOSLO revealed residual structure in only one of the two patients successfully imaged with a grade 4 EZ on OCT. In subjects with foveal atrophy (grade 5 EZ), there are unlikely to be any residual cones in the foveal center. Interestingly, a naturally occurring nonhuman primate with ACHM caused by a homozygous missense variant in *PDE6C* p.(R565Q) showed better preserved EZ in four macaques imaged with OCT (age range, 2–11 years old).[51] Given the loss of foveal EZ in all of our subjects (and all the previously reported subjects in the literature), there is likely to be a more limited therapeutic window for intervention than in other forms of ACHM, in which EZ can be relatively preserved in around 40% to 50% of the cases.[20,23] This highlights the need for deep phenotyping of affected children with *PDE6C*-associated disease and potentially milder cases that may be more amenable to functional rescue. In contrast, cones in patients with BCM can survive in reduced numbers with limited outer segment material and without waveguiding properties, suggesting the potential value of gene therapy for BCM.[52-54]

In our study, 88% of the participants were female and males were underrepresented, without, however, any expected sex-specific differences. The disorder is rare, with an estimated

prevalence of 1 in 1.25 million, and international multicenter collaborative studies may be needed to corroborate our findings and to further investigate the natural history and phenotype.

This is the first in-depth analysis, with AOSLO, international-standard full-field ERGs and S-cone ERG, and detailed clinical information, and longitudinal study including FAF and OCT of a cohort with *PDE6C*-associated ACHM. The data presented herein extend the phenotypic spectrum of ACHM, detailing some distinct features and other characteristics that are less common in *CNGA3*-, *CNGB3*-, *GNAT2*-, and *ATF6*- associated disease. Patients present with typical symptoms of ACHM but associated with slowly progressive maculopathy and with little evidence of residual macular cones in adulthood. The study suggests a limited window of therapeutic opportunity compared with cases of *CNGA3*- and *CNGB3*-ACHM.

References

1. Hirji N, Aboshiha J, Georgiou M, et al. Achromatopsia: clinical features, molecular genetics, animal models and therapeutic options. *Ophthalmic Genet*. 2018;39:1–9.

2. Aboshiha J, Dubis AM, Carroll J, et al. The cone dysfunction syndromes. *Br J Ophthalmol*. 2016;100:115–121.

3. Wissinger B, Jagle H, Kohl S, et al. Human rod monochromacy: linkage analysis and mapping of a cone photoreceptor expressed candidate gene on chromosome 2q11. *Genomics*. 1998;51:325–331.

4. Wissinger B, Gamer D, Jagle H, et al. CNGA3 mutations in hereditary cone photoreceptor disorders. *Am J Hum Genet*. 2001;69:722–737.

5. Mayer AK, Van Cauwenbergh C, Rother C, et al. CNGB3 mutation spectrum including copy number variations in 552 achromatopsia patients. *Hum Mutat*. 2017;38:1579–1591.

6. Kohl S, Baumann B, Rosenberg T, et al. Mutations in the cone photoreceptor G-protein alpha-subunit gene GNAT2 in patients with achromatopsia. *Am J Hum Genet*. 2002;71:422–425.

7. Aligianis IA, Forshew T, Johnson S, et al. Mapping of a novel locus for achromatopsia (ACHM4) to 1p and identification of a germline mutation in the alpha subunit of cone transducin (GNAT2). *J Med Genet*. 2002;39:656–660.

8. Kohl S, Zobor D, Chiang WC, et al. Mutations in the unfolded protein response regulator ATF6 cause the cone dysfunction disorder achromatopsia. *Nat Genet*. 2015;47:757–765.

9. Kohl S, Coppieters F, Meire F, et al. A nonsense mutation in PDE6H causes autosomal-recessive incomplete achromatopsia. *Am J Hum Genet*. 2012;91:527–532.

10. Chang B, Grau T, Dangel S, et al. A homologous genetic basis of the murine cpfl1 mutant and human achromatopsia linked to mutations in the PDE6C gene. *Proc Natl Acad Sci U S A*. 2009;106:19581–19586.

11. Weisschuh N, Stingl K, Audo I, et al. Mutations in the gene PDE6C encoding the catalytic subunit of the cone photoreceptor phosphodiesterase in patients with achromatopsia. *Hum Mutat*. 2018;39:1366–1371.

12. Thiadens AA, den Hollander AI, Roosing S, et al. Homozygosity mapping reveals PDE6C mutations in patients with early-onset cone photoreceptor disorders. *Am J Hum Genet*. 2009; 85:240–247.

13. Grau T, Artemyev NO, Rosenberg T, et al. Decreased catalytic activity and altered activation properties of PDE6C mutants associated with autosomal recessive achromatopsia. *Hum Mol Genet*. 2011;20:719–730.

14. Hayashi T, Kozaki K, Kitahara K, et al. Clinical heterogeneity between two Japanese siblings with congenital achromatopsia. *Vis Neurosci*. 2004;21:413–420.

15. Thiadens AA, Somervuo V, van den Born LI, et al. Progressive loss of cones in achromatopsia: an imaging study using spectral-domain optical coherence tomography. *Invest Ophthalmol Vis Sci*. 2010;51:5952–5957.

16. Aboshiha J, Dubis AM, Cowing J, et al. A prospective longitudinal study of retinal structure and function in achromatopsia. *Invest Ophthalmol Vis Sci*. 2014;55:5733–5743.

17. Hirji N, Georgiou M, Kalitzeos A, et al. Longitudinal assessment of retinal structure in achromatopsia patients with long-term follow-up. *Invest Ophthalmol Vis Sci*. 2018; 59:5735–5744.

18. Genead MA, Fishman GA, Rha J, et al. Photoreceptor structure and function in patients with congenital achromatopsia. *Invest Ophthalmol Vis Sci*. 2011;52:7298–7308.

19. Sundaram V, Wilde C, Aboshiha J, et al. Retinal structure and function in achromatopsia: implications for gene therapy. *Ophthalmology*. 2014;121:234–245.

20. Langlo CS, Patterson EJ, Higgins BP, et al. Residual foveal cone structure in *CNGB3*-associated achromatopsia. *Invest Ophthalmol Vis Sci*. 2016;57:3984–3995.

21. Spaide RF, Curcio CA. Anatomical correlates to the bands seen in the outer retina by optical coherence tomography: literature review and model. *Retina*. 2011;31:1609–1619.

22. Jonnal RS, Kocaoglu OP, Zawadzki RJ, et al. The cellular origins of the outer retinal bands in optical coherence tomography images. *Invest Ophthalmol Vis Sci*. 2014;55:7904–7918.

23. Georgiou M, Litts KM, Kalitzeos A, et al. Adaptive optics retinal imaging in CNGA3-associated achromatopsia: retinal characterization, interocular symmetry, and intrafamilial variability. *Invest Ophthalmol Vis Sci*. 2019;60:383–396.

24. Georgiou M, Kalitzeos A, Patterson EJ, et al. Adaptive optics imaging of inherited retinal diseases. *Br J Ophthalmol*. 2018; 102:1028–1035.

25. Roorda A, Williams DR. The arrangement of the three cone classes in the living human eye. *Nature*. 1999;397:520–522.

26. Dubra A, Sulai Y, Norris JL, et al. Noninvasive imaging of the human rod photoreceptor mosaic using a confocal adaptive optics scanning ophthalmoscope. *Biomed Opt Express*. 2011; 2:1864–1876.

27. Rossi EA, Chung M, Dubra A, et al. Imaging retinal mosaics in the living eye. *Eye (Lond)*. 2011;25:301–308.

28. Scoles D, Sulai YN, Langlo CS, et al. *In vivo* imaging of human cone photoreceptor inner segments. *Invest Ophthalmol Vis Sci*. 2014;55:4244–4251.

29. Abozaid MA, Langlo CS, Dubis AM, et al. Reliability and repeatability of cone density measurements in patients with congenital achromatopsia. *Adv Exp Med Biol*. 2016;854:277–283.

30. Langlo CS, Erker LR, Parker M, et al. Repeatability and longitudinal assessment of foveal cone structure in CNGB3-associated achromatopsia. *Retina*. 2017;30:1956–1966.

31. Tee JJL, Carroll J, Webster AR, Michaelides M. Quantitative analysis of retinal structure using spectral-domain optical coherence tomography in RPGR-associated retinopathy. *Am J Ophthalmol*. 2017;178:18–26.

32. Mastey RR, Georgiou M, Langlo CS, et al. Characterization of retinal structure in ATF6-associated achromatopsia. *Invest Ophthalmol Vis Sci* 2019;60:2631–2640.

33. McCulloch DL, Marmor MF, Brigell MG, et al. ISCEV standard for full-field clinical electroretinography (2015 update). *Doc Ophthalmol*. 2015;130:1–12.

34. Bach M, Brigell MG, Hawlina M, et al. ISCEV standard for clinical pattern electroretinography (PERG): 2012 update. *Doc Ophthalmol*. 2013;126:1–7.

35. Audo I, Michaelides M, Robson AG, et al. Phenotypic variation in enhanced S-cone syndrome. *Invest Ophthalmol Vis Sci*. 2008;49:2082–2093.

36. Simunovic MP, Votruba M, Regan BC, Mollon JD. Colour discrimination ellipses in patients with dominant optic atrophy. *Vision Res*. 1998;38:3413–3419.

37. Dubra A, Sulai Y. Reflective afocal broadband adaptive optics scanning ophthalmoscope. *Biomed Opt Express*. 2011;2:1757–1768.

38. Salmon AE, Cooper RF, Langlo CS, et al. An automated reference frame selection (ARFS) algorithm for cone imaging with adaptive optics scanning light ophthalmoscopy. *Trans Vis Sci Tech*. 2017;6(2):9.

39. Dubra A, Harvey Z. *Registration of 2D Images from Fast Scanning Ophthalmic Instruments*. Berlin, Heidelberg: Springer Berlin Heidelberg, 2010.

40. Davidson B, Kalitzeos A, Carroll J, et al. Fast adaptive optics scanning light ophthalmoscope retinal montaging. *Biomed Opt Express*. 2018;9:4317–4328.

41. Rentzsch P, Witten D, Cooper GM, et al. CADD: predicting the deleteriousness of variants throughout the human genome. *Nucleic Acids Res* 2018;47:D886–D894.

42. Thomas MG, Kumar A, Kohl S, et al. High-resolution in vivo imaging in achromatopsia. *Ophthalmology*. 2011;118:882–887.

43. Xu M, Gelowani V, Eblimit A, et al. ATF6 is mutated in early onset photoreceptor degeneration with macular involvement. *Invest Ophthalmol Vis Sci* 2015;56:3889–3895.

44. Vincent A, Robson AG, Neveu MM, et al. A phenotype-genotype correlation study of X-linked retinoschisis. *Ophthalmology*. 2013;120:1454–1464.

45. Wilk MA, McAllister JT, Cooper RF, et al. Relationship between foveal cone specialization and pit morphology in albinism. *Invest Ophthalmol Vis Sci*. 2014;55:4186–4198.

46. Michaelides M, Aligianis IA, Holder GE, et al. Cone dystrophy phenotype associated with a frameshift mutation (M280fsX291) in the alpha-subunit of cone specific transducin (GNAT2). *Br J Ophthalmol*. 2003;87:1317–1320.

47. Gardner JC, Liew G, Quan YH, et al. Three different cone opsin gene array mutational mechanisms with genotype-phenotype correlation and functional investigation of cone opsin variants. *Hum Mutat*. 2014;35:1354–1362.

48. Stearns G, Evangelista M, Fadool JM, Brockerhoff SE. A mutation in the cone-specific pde6 gene causes rapid cone photoreceptor degeneration in zebrafish. *J Neurosci*. 2007; 27:13866–13874.

49. Michaelides M, Johnson S, Simunovic MP, et al. Blue cone monochromatism: a phenotype and genotype assessment with evidence of progressive loss of cone function in older individuals. *Eye (Lond)*. 2005;19:2–10.

50. Robson AG, Michaelides M, Luong VA, et al. Functional correlates of fundus autofluorescence abnormalities in patients with RPGR or RIMS1 mutations causing cone or cone rod dystrophy. *Br J Ophthalmol*. 2008;92:95–102.

51. Moshiri A, Chen R, Kim S, et al. A nonhuman primate model of inherited retinal disease. *J Clin Invest*. 2019;129:863–874.

52. Cideciyan AV, Hufnagel RB, Carroll J, et al. Human cone visual pigment deletions spare sufficient photoreceptors to warrant gene therapy. *Hum Gene Ther*. 2013;24:993–1006.

53. Carroll J, Dubra A, Gardner JC, et al. The effect of cone opsin mutations on retinal structure and the integrity of the photoreceptor mosaic. *Invest Ophthalmol Vis Sci*. 2012;53:8006–8015.

54. Patterson EJ, Kalitzeos A, Kasilian M, et al. Residual cone structure in patients with X-linked cone opsin mutations. *Invest Ophthalmol Vis Sci*. 2018;59:4238–4248.